

Ab Initio Study of Sorption on Pyrophyllite: Structure and Acidity of the Edge Sites

Sergey V. Churakov

Paul Scherrer Institute, CH-5232 Villigen PSI, Switzerland

Received: July 14, 2005; In Final Form: January 4, 2006

Pyrophyllite, $\text{Al}_2[\text{Si}_4\text{O}_{10}](\text{OH})_2$, is the simplest structural prototype for 2:1 dioctahedral phyllosilicates. Since it does not possess permanent structural charge as other clay minerals do, it is used to investigate sorption properties of the clay surfaces not related to the permanent structural charge. The bulk structure and surface geometries of pyrophyllite have been modeled using an orthorhombic constrained supercell. The results of the calculations are in excellent agreement with available experimental data and earlier ab initio simulations. It is shown that the symmetry-constrained model is able to accurately reproduce the basic structural characteristic of pyrophyllite. The electrostatic potential near the (001) surface was used to analyze a possible scenario for the water sorption on the basal plane of pyrophyllite. The calculations predict a slightly hydrophobic behavior of the basal plane. The hydronium ion was found to form a strongly bonded conformation in the siloxane cavity. The relative stability and composition of lateral facets of pyrophyllite have been studied using the supercell approach. The crystals of pyrophyllite are predicted to have a prismatic habit dominated by (110) and (-110) edge facets and basal plane. On the basis of the Fukui functions and the relative protonation/deprotonation enthalpies, the relative acidity and density of the reactive surface sites have been predicted. The $\equiv\text{Al}-\text{O}-\text{Si}\equiv$ sites have the highest proton affinity on the (100), (110), and (130) facets and three line sign $\text{Al}-\text{OH}$ groups on the (010) edges. The deprotonation of the $\equiv\text{Al}-\text{OH}_2$ sites is followed by $\equiv\text{Al}-\text{OH}$ and $\equiv\text{Si}-\text{OH}$ groups. The calculations suggest a new scale for acidities of edge sites in pyrophyllite that should facilitate the thermodynamic modeling of the sorption processes in compacted clays.

Introduction

Clay minerals occur as colloidal aggregates of tiny particles. Their large surface area is responsible for a number of unique physical and chemical properties such as swelling, cation exchange, and pH-dependent sorption.¹ Because of their strong metal retardation characteristics, clay sediments are considered as potential host rocks for radioactive waste repositories. Increased competence in the safety and performance of such repositories can be achieved by demonstrating a good understanding of the mechanisms controlling the radionuclide mobility and retardation in clays.

The basic structural element of phyllosilicates can be imagined as a hexagonally ordered layer of octahedra sandwiched between two tetrahedral siloxane layers, commonly referred to as a TOT layer. Various isomorphic substitutions in the octahedral and tetrahedral layers of the clay minerals result in a permanent structural charge of the TOT unit. The excess charge is compensated by counterions in the interlayer, which are predominantly the alkali metals. The basal plane of the TOT layer is chemically inert, and the affinity of the interlayer ions to the water is stronger than to the basal surface. The water molecules penetrate into the clays, splitting the TOT units apart in order to accomplish the hydration shell of the ions in the interlayer. The process is known as swelling and has been studied both experimentally and by molecular modeling techniques.^{2–7}

In contrast to the basal plane, the edges of clay particles are extremely reactive. Their sorption properties show chemical

similarities to the behavior of Si oxides and Al hydroxides. The experimental studies of crystal growth kinetics have proven the dissolution/precipitation processes to take place exclusively on the edge sites of the TOT layer.^{8,9} In excess of fluid phase, the mechanism of dissolution and precipitation is controlled by pH in the solution. In the acidic environment, the octahedral layers dissolve first, while in high pH solutions, the tetrahedral layers can be dissolved more easily.¹⁰ The structure, composition, and charge on the edges change as a function of pH because of the dynamic proton exchange between the surface of the clay and the coexisting aqueous solution. In compacted clays, where the contribution of solid phases substantially exceeds the volume of fluid, the thermodynamic equilibria at the liquid–clay interface control the composition of the interstitial water. Distinct lateral facets of the clay minerals are composed of functional groups with different protonation constants and site densities.¹¹ Thus, the composition of the pore fluid in compacted systems should also depend on the relative stability of the various facets of clay.

Experimental studies^{8–17} clearly illustrate that the mechanism of the metal sorption on clays is dependent on the pH. In acidic solutions, the uptake of the cations preferentially takes place by the cation exchange mechanism. At high pH, the composition of the lateral facets changes to favor the formation of strongly bonded cation complexes at the edge sites. Accurate description of the sorption processes and the chemically validated modeling of the experimental data require an understanding of the surface chemistry at the edges and the reactivity and capacity of the surface sites. The missing data on the density of reactive sites, their protonation constants, surface composition, and relative

* E-mail: sergey.churakov@psi.ch. Telephone: +41 56 310 4113. Fax: +41 56 310 2821.

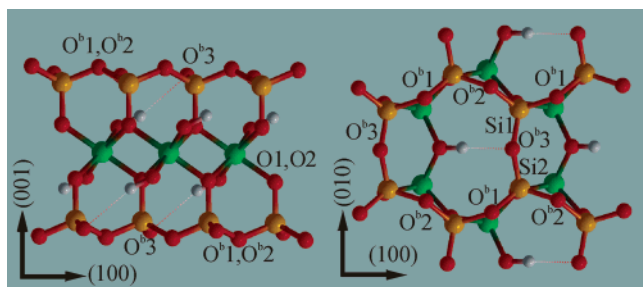


Figure 1. The crystal structure of pyrophyllite. Oxygen atoms are red, aluminum, green; light brown, silicon; and hydrogen, gray.

stability can be obtained by combining experimental measurements spectroscopy and molecular modeling.

Different macroscopic models for the surface complexation have been proposed to describe the sorption of cations on clays from aqueous solutions.^{12,13,18–20} Most of them consider two major contributions to the electrostatic potential, namely, the electric field produced by the permanent structural charge in the TOT layer and a pH-dependent potential due to proton sorption/desorption at edge sites. Both contributions are considered in the mean field sense and to the first approximation can be treated as additive. The electrostatic potential due to the permanent structural charge is straightforward to calculate, since it is determined by the extent of the isomorphic substitution in the TOT layer only. An accurate estimation of the pH-dependent potential requires several fundamental parameters which are poorly, if at all, constrained: (1) the effective surface area and the structure of the edge sites; (2) the density of sites involved in the protonation/deprotonation reactions; (3) the equilibrium absorption constants for the reactive sites. The main purpose of this paper is to constrain these parameters on the basis of the ab initio calculations.

Pyrophyllite, $\text{Al}_2[\text{Si}_4\text{O}_{10}](\text{OH})_2$, is the simplest structural prototype for 2:1 dioctahedral phyllosilicates (Figure 1). Two-thirds of the available octahedral sites are occupied by aluminum atoms, and silicon atoms are situated in the tetrahedral sites. In contrast to the other clay minerals, pyrophyllite does not possess a permanent electric charge in the TOT layer. Thus, pyrophyllite is the simplest model for a large variety of clays that can be used to study sorption properties of the clays not related to the permanent structural charge. Therefore, the pyrophyllite has been intentionally chosen for this study to exclude the influence of the structural charge.

The paper is organized as follows: The simulation setup was first validated by performing calculations of the bulk structure of pyrophyllite. The electrostatic potential near the basal plane was used to analyze the interaction of the basal plane with the water and the hydronium ion. On the basis of the results of static calculations, the structure and acid–base reactivity of the edge sites on pyrophyllite were investigated. The structure and surface energy of distinct lateral facets in pyrophyllite as function of the water coverage are predicted. The reactivity of the surface sites is estimated on the basis of the Fukui indexes²¹ and the direct calculations of the relative protonation/deprotonation enthalpies. Finally, a new scale for acidity of the surface sites is proposed.

Methods

For all the calculations in this work, we use the density functional theory^{22,23} (DFT) with generalized gradient approximation PBE²⁴ for the exchange and correlation functionals. The interaction of the valence electrons with the core states is

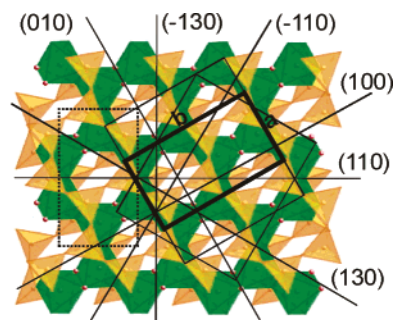


Figure 2. Top view of the TOT element of pyrophyllite in [001] direction. Silicon tetrahedra are shown in orange. The octahedral sites occupied by Al are shown in green. Small red spheres at the edges of the octahedral sites represent OH groups. Dotted lines indicate the conventional choice of the unit cell for pyrophyllite. The unit cell used in this work to assign indexes of atomic planes is indicated by bold solid lines. The parameters of the unit cell are given in Table 1. The supercells for the surface calculations are indicated by thin solid lines.

described by the pseudopotential formalism. We use ultrasoft Vanderbilt-type pseudopotentials,²⁵ which allow us to decrease the required basis set dramatically. The wave functions of the valence electrons are expanded into plane wave basis set up to the 25 Ry cutoff energy. The ab initio Car–Parrinello molecular dynamics (MD) simulations²⁶ were performed, with a time step of 0.17 fs and a fictitious electron mass of 500 au. For the charged systems, a homogeneous neutralizing background was added to maintain the charge neutrality in the supercell. The accuracy and transferability of the pseudopotentials as well as the convergence of the plane wave basis set expansion were tested against the geometry of small molecules and simple oxides. The bond length in the molecules and the lattice parameters of solids could be reproduced within 1% and 2% of the experimental values, respectively.

Bulk Structure of Pyrophyllite and Supercell Geometry.

Stacking of the TOT layers in pyrophyllite results in a wide range of polymorphism. Natural samples mainly occur as an *1Tc* prototype, which belongs to the centric space group $C\bar{1}$.^{27,28} The monoclinic *2M* prototype with the $C2/c$ space group is also common for pyrophyllite. The low symmetry of the lattice gives rise to complexity in computer simulations. Because the deviation from orthogonality of the α and γ angles is very small and a monoclinic polymorph of pyrophyllite exists, it might be reasonable to constrain these angles at 90° . The value of the β angle is determined by the electrostatic and van der Waals interactions between neighboring TOT layers. Since the van der Waals interaction is not properly accounted for in the DFT calculations, and it is technically advantageous to work with the orthogonal supercell, the lattice dimension in the *c* direction was increased from the experimentally reported value of 9.0 Å to a value of 12 Å, and the β angle fixed at 90° . In this way, we expect to exclude ill-described interactions between neighboring TOT units and maintain the correct structure of the TOT layer in an orthorhombic supercell. Test calculations have confirmed that a further increase of the *c* spacing does not show any influence on the structure geometry. Calculations were performed on a $2 \times 1 \times 1$ supercell with a single *k*-point in the center of the Brillouin zone. This supercell corresponds to a simulation performed on a single unit cell with (0, 0, 0) and $(\pi/a, 0, 0)$ *k*-points in the Brillouin zone. Earlier studies of the pyrophyllite crystal chemistry have shown that two *k*-points are sufficient for both energy and stress calculations.²⁹ The $2 \times 1 \times 1$ supercell contains four formula units of pyrophyllite. The orientation of the supercell is shown in Figure 2. To test the convergence with respect to *k*-points, an additional calculation

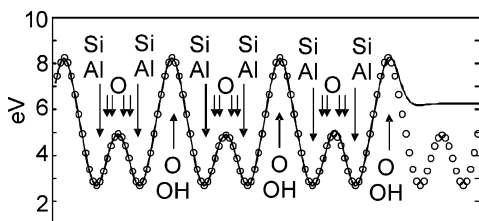


Figure 3. Electrostatic potential for the relaxed (010) surface of pyrophyllite (solid line) and the potential in the bulk (open circles). The potential has been averaged parallel to the surface and plotted from the center of the slab to the point deep within the vacuum.

was performed with the $4 \times 2 \times 1$ supercell. No structural changes were observed relative to the smaller $2 \times 1 \times 1$ supercell, which has been used throughout the study.

Simulation of the Edge Sites. To model a semi-infinite bulk system with an exposed surface, we use a 3D periodically repeated box containing a slab of several atomic layers. Above the slab, we add at least 6 Å of vacuum space to reduce the interaction with the periodic images. The other parameters of the supercell were taken from the geometry optimization of bulk pyrophyllite. The orientations of the supercells for different edges are shown in Figure 2. To ensure sufficient separation of the periodic slices, the calculations were repeated by decoupling electrostatic images in the Poisson solver using Hockney's method.³⁰ Both methods predict the same geometry, validating the accuracy of the supercell approach. To ensure that the surface geometry is not affected by the thickness of the atomic layers representing the bulk structure, the calculations were repeated with a $2 \times$ thicker slab, containing eight structural units of pyrophyllite. No changes in the surface geometry were observed. In Figure 3, an example of electrostatic potential averaged in the plane normal to the [010] vector obtained from the test slab calculation is superimposed with the respective value for the bulk structure. The plot illustrates that the bulk potential perfectly coincides with that in the bulk region. Even at the outermost Al and Si atoms, the surface potential is almost identical to the bulk, suggesting that the surface relaxations efficiently compensate the distortions caused by the formation of the facet. The first significant deviation from the bulk potential is observed just beyond the outermost layer of oxygen sites. In the vacuum area, the surface potential reaches a constant value, proving that the periodic images are sufficiently separated.

Surface energy of the edges, E_{surf} , as a function of the water coverage was calculated as follows:

$$E_{\text{surf}} = \frac{E_{\text{surf}}^{\text{prl}} - (E_{\text{bulk}}^{\text{prl}} + n \times E_{\text{gas}}^{\text{H}_2\text{O}})}{A} \quad (1)$$

where $E_{\text{gas}}^{\text{H}_2\text{O}}$ is the water energy in the gas phase, $E_{\text{bulk}}^{\text{prl}}$ the energy of the bulk pyrophyllite, $E_{\text{surf}}^{\text{prl}}$ the energy of the pyrophyllite with water absorbed on the surface, A is the surface area and n the number of water molecules involved in sorption. The accuracy of the calculated surface energies is ± 1 meV/Å².

Site Reactivity. Frontier electron theory of chemical reactivity can be rationalized from the density functional theory of the electronic structures of molecules.^{21,31,32} The Fukui function, $f(r)$, is defined as a local response of the system on the change in number of electrons

$$f(r) = [\delta\rho(r)/\delta N]_{v(r)} \quad (2)$$

where $\rho(r)$ is the electron density, N is the number of electrons, and $v(r)$ is the electrostatic potential. With the finite difference approximation, two functions $f^+(r)$ and $f^-(r)$ can be defined

which characterize the nucleophilic and the electrophilic attack, respectively

$$f^+(r) = \rho_{N+1}(r) - \rho_N(r) \quad (3)$$

$$f^-(r) = \rho_N(r) - \rho_{N-1}(r) \quad (4)$$

where $\rho_{N+1}(r)$, $\rho_N(r)$, and $\rho_{N-1}(r)$ are the electron densities of the system with $N + 1$, N , and $N - 1$ electrons, respectively. To characterize the reactivity of particular sites, the differential electron density should be partitioned between atoms in the system. Integration over atomic regions leads to the atom's electronic population. In this work, the Fukui indexes for atomic site i were calculated as the difference of effective atomic charges (q_i) for the systems with $N + 1$, N , and $N - 1$ electrons

$$f_i^+ = -[q_i(N + 1) - q_i(N)] \quad (5)$$

$$f_i^- = -[q_i(N) - q_i(N - 1)] \quad (6)$$

The population analysis is not a unique procedure and can be performed in different ways.^{33–35} We rely on the Stockholder charges,³⁵ which were shown to be superior to other partitioning techniques while guaranteeing nonnegativity of the Fukui indexes.³⁶

Bond Valence Theory. The bond valence theory³⁷ has been shown to be successful in predicting the equilibrium bond structure in simple solid phases and molecules. The theory is based on the empirical correlation between bond strength and bond length in inorganic crystals. The bond valence s_{ij} is calculated as

$$s_{ij} = \exp[(r_0 - r_{ij})/B] \quad (7)$$

where r_{ij} is the interatomic distance, and r_0 and B are bond-specific fitting parameters. The r_0 and B were fitted by Brown (ref 37, Table A1.1) for a number of bonds using the Inorganic Crystal Structure Database. The B values were found to be universal for different bond types, while r_0 varies significantly for various atomic pairs. Equation 7 gives satisfactory results for all bond types except hydrogen bonding. A three-parameter equation was found to give a satisfactory description for hydrogen bonds

$$s_{ij} = e/(r_{ij} - f) - g \quad (8)$$

where e , g , and f are the fitting parameters (eq A1.2 in ref 37). The calculation should include both the short and long parts of the hydrogen bond up to 3.0 Å. The bond valence theory postulates that in a stable structure the sum of the bond valences should be equal to the formal valence of the atom

$$(V_i - \sum_j s_{ij})^2 \rightarrow 0 \quad (9)$$

where the index j is running over all sites in the first coordination shell of the atom i .

The more the bond valence deviates from the formal atomic valence, the lower the expected stability of this atom. On the basis of this observation, correlations between the bond valence deficiency and the acidity of the oxygen sites have been proposed.^{19,20}

Results and Discussion

Lattice Geometry and Structure of the TOT Layer. Since we are using several constraints and simplifications for the

TABLE 1: Experimentally Determined Lattice Parameters of Pyrophyllite and the Theoretically Calculated Lattice Constants at Zero Pressure and Temperature^a

	<i>a/b/c</i>	$\alpha/\beta/\gamma$
Lee and Guggenheim (1981) (experimental)	5.160 8.966 9.347	91.18(4) 100.46(4) 89.64(3)
MacKenzie et al. (1985) (experimental)	5.20 9.15 9.45	92.0 98.83 89.0
Refson et al. (2003) ^b (ab initio calculations)	5.218 9.079 10.001	90.49 101.73 89.69
Bickmore et al. (2003) (ab initio calculations)	5.1488 8.9979 9.8409	91.20 100.74 89.66
this work (ab initio calculations)	5.219 (1.1%) 9.033 (0.7%) 12.0 ^c	90 ^c 90 ^c 90 ^c

^a The lattice geometry was fixed as having orthorhombic symmetry. The *c* dimension was constrained at 12.0 Å. The values in the brackets give the deviation of the theoretical values from the data of Lee and Guggenheim.²⁷ ^b Data reported in the table correspond to GeOpt 2 calculation.^{29,24} Table 1. ^c The values were fixed during calculations.

TABLE 2: Calculated and Experimental Interatomic Distances and Bond Valence Parameters (eqs 7, 8) in Pyrophyllite^a

	Refson et al. (2003)	Lee and Guggenheim (1981)	this work			
	<i>r</i> , [Å]	<i>r</i> , [Å]	<i>s</i> _{ij} ^B	<i>r</i> , [Å]	<i>s</i> _{ij} ^B	<i>s</i> _{ij} ^{DFT}
Al–O1, O2	1.95	1.921	0.443	1.939	0.422	0.486
Al–O3(OH)	1.91	1.889	0.483	1.901	0.468	0.538
Si–O ^a	1.66	1.633	0.976	1.652	0.927	0.945
Si–O ^b 3	1.635	1.616	1.022	1.633	0.976	0.994
Si1–O ^b 1, Si2–O ^b 2	1.63	1.604	1.056	1.629	0.987	1.005
O–H	0.974			0.972	0.942	0.925
Σ <i>s</i> _{Si–O}			4.075		3.866	3.939
Σ <i>s</i> _{Al–O}			2.740		2.625	3.020
Σ <i>s</i> _{H–O}					1.105	1.079
Σ <i>s</i> _{O–Me}					1.910	1.997

^a The *s*_{ij}^B are the bond valence values calculated using data of Brown (2002). The *s*_{ij}^{DFT} are the bond valence values calculated with parameters fitted to the ab initio structure of pyrophyllite (see text for details).

pyrophyllite lattice, the ability of our calculations to reproduce structural features of the bulk pyrophyllite is a critical test for the reliability of the surface simulations. We search for the global minimum of the lattice energy of pyrophyllite, varying the lattice parameters *a* and *b* for a constant *c* dimension and orthorhombic symmetry of the supercell. Results of the calculations (Table 1) are compared with experimental data and other ab initio simulations. The calculated values for *a* and *b* lattice parameters are ~1% larger than the experimentally observed values. Similar deviations of lattice parameters were reported by Refson et al.,²⁹ who performed the calculation with another exchange-correlation functional but allowed for the triclinic symmetry of the unit cell. The small positive deviation of the lattice parameters can be attributed to the accuracy of gradient-corrected exchange-correlation functionals, which are known to systematically overestimate the bond length and lattice constants of solids.^{29,38} The calculation of Bickmore²⁰ seems to have much better agreement with the experimental data, even though they have been performed under conditions similar to the simulations of Refson et al.²⁹ The discrepancy might be due

TABLE 3: Structural Distortion of the TOT Layer in Pyrophyllite (see eqs 10–14)

	this work	Refson et al. (2003) (ab initio calculations)	Lee and Guggenheim (1981) (experimental)
<i>T</i> _{rot} [°]	10.17	10.07	10.2
AO [Å]	3.038	3.04	3.00
<i>T</i> _d [Å]	2.186	2.18	2.153
ψ [deg]	57.08	56.72	57.1
<i>O</i> _h [Å]	2.105	2.126	2.08
<i>T</i> _{tilt} [°]	6.58	6.7	7.0
∠OH _{out of plane}	25.33	25.43	

to different strategies for generating the pseudopotentials in both studies.

The calculated interatomic distances in pyrophyllite are summarized in Table 2. Similar to the fully relaxed optimization of Refson et al.,²⁹ the calculations are in good agreement with the experimental data of Lee and Guggenheim,²⁷ with an average positive deviation of 0.02–0.03 Å. In contrast, the calculations of Bickmore²⁰ predict, on average, that the Si–O and Al–O bonds are too short by ~0.01 Å.

The deviation of the calculated bond lengths is a direct consequence of the mismatch of the lattice parameters, which can be attributed to the systematic errors in the pseudopotentials and exchange-correlation functionals. A comparison of the bond angles usually provides a finer test for the performance of the calculations. The following structural characteristics of the tetrahedral and octahedral distortions in the TOT layer were calculated:²⁹

$$T_{\text{rot}} [\text{deg}] = \frac{1}{2} [120^\circ - \angle \text{O}_b \text{O}_b \text{O}_b] \quad (10)$$

$$\text{AO} [\text{Å}] = \frac{2\langle R_{\text{Oo}_{\text{tet}}} \rangle}{\sqrt{3}} \cos(T_{\text{rot}}) \quad (11)$$

$$T_d [\text{Å}] = [\langle z_{\text{O}_b} \rangle - \langle z_{\text{O}_a} \rangle] \csc(\beta) \quad (12)$$

$$\psi [\text{deg}] = \cos^{-1} \left[\frac{1}{2} O_h \div \langle R_{\text{AlO(OH)}} \rangle \right] \quad (13)$$

$$T_{\text{tilt}} [\text{deg}] =$$

mean tilt angle between basal faces of adjacent tetrahedra
(14)

where *O*_h is the thickness of the octahedral layer, and *z*_{O_b} and *z*_{O_a} are the *z* coordinates of the basal and apical oxygen atoms, respectively. The calculations show an excellent agreement with the experimental data and earlier ab initio studies (Table 3). Remarkably, the results show that the structural parameters of the pyrophyllite can be reproduced using a constrained orthorhombic supercell. Therefore, we can take full advantage of the orthorhombic cell in the calculations.

Ab Initio Geometries and Bond Valence Theory. The bond valence theory has proven to be a powerful tool for predicting crystals structure and relative bond strength. Recently, the bond valence theory has been applied to predict the acidity of surfaces and inorganic molecules.^{19,20} It would be convenient to apply the method directly to the results of ab initio crystal structure refinement. The obstacle to this approach is a systematic deviation of bond length predicted by ab initio simulations from the experimental data.

The calculated bond valence sums for the experimental and ab initio structure of pyrophyllite are given in Table 2. The total

bond strength of the silicon atom is in reasonable agreement with the formal charge on the silicon. In contrast, the bond strength of the aluminum is substantially underestimated in comparison to both the experimental and ab initio bond distances (Table 2). The underestimated bond strength is an indication of bond distances which are too long. Since ab initio calculations predict longer bond lengths, the deviation is even more significant. Original parameters for the bond valence equations have been fitted to a large number of structures in the Inorganic Crystal Structure Database. The equilibrium geometry of the Al–O bonds in the octahedral layer of pyrophyllite seems to be too different from the typical structures used for the calibration. The discrepancy can be resolved by refitting bond valence parameters directly to the ab initio data. In such a way, we obtain parameters for the bond valence equations consistent with the possible systematic uncertainties of ab initio calculations. The new parameters are specific to pyrophyllite, but more reliable for the analysis of its surface reactivity than the original dataset.

We find that the best agreement with the formal valence of the Si, Al, O, and H can be obtained when using r_0 in eq 7 equal to 1.631 and 1.672 Å for Si–O and Al–O bonds, respectively, and the f parameter in eq 8 set to 0.594 Å. The original bond valence parameters were 1.624, 1.62, and 0.6 Å, respectively. The new parameters for the Si–O and O–H bonds are very similar to the data in Brown's dataset.³⁷ Our parametrization for the Al–O bond turns out to be in better agreement with the alternative calibration of Alleman³⁹ who estimated r_0 to 1.644 Å. Total bond valence strengths for Al, Si, O, and H atoms of pyrophyllite are summarized in Table 2. The formal valence can be reproduced within an accuracy of 2%. The new dataset is used to evaluate the acidity of surface sites on the edges of pyrophyllite.

Structure and Surface Energy of the Edge Facets in Pyrophyllite. To avoid possible confusion, one should agree on indexing the atomic planes in pyrophyllite. The basic structural elements of triclinic pyrophyllite and the other clay minerals such as montmorillonite are similar. However, these two phases have different symmetry and different conventional unit cells. In the case of the orthogonally constrained supercell that is used in the simulations, both montmorillonite-like and conventional pyrophyllite-like orientation of the unit cell can be applied. Similar to the work of Bickmore,²⁰ the Miller indexes of atomic planes in pyrophyllite are assigned according to the montmorillonite-like orientation of the supercell. The correspondence between pyrophyllite and the montmorillonite-like unit cell and the Miller indexes of atomic planes is established in Figure 2.

According to the basic crystallographic principles, the most common facets are represented by the crystallographic planes with maximal atomic density.¹¹ The lateral facets of pyrophyllite with highest atomic density are indicated in Figure 2. In the triclinic pyrophyllite structure, there are six nonequivalent lateral atomic planes (100), (010), ($\bar{1}10$), (110), ($\bar{1}30$), and (130). Since the cell geometry is constrained, the (130) plane is equivalent to the ($\bar{1}30$) facet, and (110) is identical to ($\bar{1}10$). Therefore, only four surfaces, namely, (100), (010), (110), and (130), need to be considered.

The lateral facets are formed by cutting the crystal parallel to the selected direction and keeping the crystal's stoichiometry unchanged. Broken Si–O and Al–O bonds and undercoordinated surface polyhedra newly formed through this procedure are extremely reactive and play the role of absorption sites. In

TABLE 4: Surface Energies (E_{surf}) of Pyrophyllite Facets for Different Water Coverage (eq 1)^a

	unit area [nm ²]	$E_{\text{surf}} \times 2\text{H}_2\text{O}$ [meV/Å ²]	$E_{\text{surf}} \times 4\text{H}_2\text{O}$ [meV/Å ²]	$\Delta H_{\text{sorb}}^{\text{H}_2\text{O}}$ [kcal mol ⁻¹]
(010)	1.25	11.8	5.4	−9.3
(100)	1.08	13.0	1.9	−13.8
(110)	1.25	12.2	1.6	−13.9
(130)	1.08	12.2	5.7	−8.1

^a The first two water molecules per unit area are chem-sorbed through dissociation mechanism ($E_{\text{surf}} \times 2\text{H}_2\text{O}$, low water coverage). The next two molecules are phys-sorbed in molecular form ($E_{\text{surf}} \times 4\text{H}_2\text{O}$, high water coverage). $\Delta H_{\text{sorb}}^{\text{H}_2\text{O}}$ gives the enthalpy of phys-sorbed water.

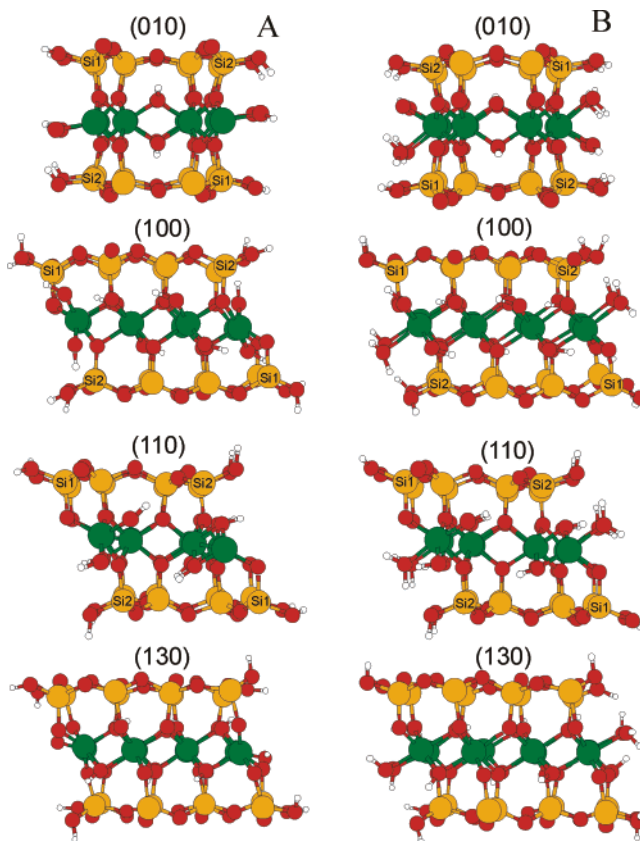


Figure 4. Structure of edge sites at low (A) and high (B) water coverage. The Si atoms are shown in orange. The Al atoms are indicated by green color. The oxygen sites are shown in red. The hydrogen atoms are depicted as white spheres. Nonequivalent Si–OH sites are indicated.

the presence of water, the stabilization of the lateral facets is achieved through disassociative sorption of H₂O molecules. The dangling Si–O and Al–O bonds are saturated with protons. The undercoordinated Si and Al atoms complete their coordination shell with OH groups. Two H₂O molecules per unit of surface area (Table 4) are required to compensate dangling bonds on the edge sites. After saturation, all dangling bonds of the surface Si atoms are four-coordinated, and the surface Al sites are five-coordinated. Optimized geometries of these configurations are shown in Figure 4a. The energies of different facets are listed in the second column of Table 4. The bond lengths and bond valence sums for the surface sites are summarized in Table 5. Hereafter, these configurations are referred to as those with low water coverage. The surface energies of different facets turned out to be all the same within the accuracy of the calculations. The results suggest that both facets have almost equivalent stability and refresh a long-standing discussion on crystal chemistry of the edge sites in phyllosilicates.^{8,11,20,40}

TABLE 5: Structural Parameters of the Surface Groups on Pyrophyllite at Low Water Coverage ($2 \times \text{H}_2\text{O}$ per unit area)^a

	$\Sigma s_{\text{O-Me}}$	Me-O $R [\text{\AA}^2]/s_{ij}^{\text{DFT}}$	O-H $R [\text{\AA}^2]/s_{ij}^{\text{DFT}}$	q_{O}	f^-	f^+
(010)						
Si1-OH	1.917	1.634/0.993	0.972/0.925	-0.110	0.009	0.005
Si2-OH	1.894	1.630/1.004	0.984/0.890	-0.118	0.028	0.005
Al-OH	1.822	1.749/0.813	0.972/0.925	-0.170	0.031	0.003
			2.276/0.084			
Si-O-Al ₂	2.101	1.657/0.933		-0.088	0.010	0.002
		1.880/0.570				
		1.906/0.531				
(100)						
Si1-OH	1.891	1.652/0.945	0.972/0.924	-0.119	0.028	0.003
Si2-OH	1.942	1.648/0.954	0.972/0.924	-0.103	0.007	0.004
Al-(OH)-Al	2.075	1.872/0.582	0.977/0.911	-0.059	0.003	0.003
Si-O-Al	1.874	1.619/1.033		-0.180	0.028	0.002
		1.761/0.787				
(110)						
Si1-OH	1.918	1.633/0.995	0.973/0.923	-0.109	0.004	0.006
Si2-OH	1.896	1.642/0.970	0.972/0.926	-0.117	0.026	0.004
Al-(OH)-Al	2.005	1.892/0.552	1.207/0.824	-0.076	0.013	0.002
		1.673/0.629				
Si-O-Al	1.835	1.619/1.034	2.713/0.034	-0.185	0.040	0.003
		1.770/0.768				
(130)						
Si1-OH	1.925	1.630/1.003	0.973/0.922	-0.105	0.004	0.005
Si2-OH	1.957	1.642/0.970	0.973/0.922	-0.096	0.004	0.006
			2.417/0.065			
Si1-OH	1.896	1.642/0.971	0.972/0.925	-0.113	0.017	0.004
Si2-OH	1.889	1.631/1.001	0.985/0.888	-0.117	0.031	0.005
Al-OH	1.842	1.744/0.822	0.971/0.927	-0.166	0.034	0.004
			2.211/0.094			
Si-O-Al	1.801	1.625/1.017		-0.186	0.040	0.002
		1.771/0.766				
Al-(OH)-Al	1.987	1.875/0.577	0.975/0.915	-0.077	0.017	0.003
		1.932/0.495				

^a $\Sigma s_{\text{O-Me}}$ is the bond valence sum on oxygen atoms. Me-O is the cation-oxygen distance and bond strength calculated with eq 7. O-H is the hydrogen bond length and the bond valence contribution (eq 8). Several values are given for nonequivalent bonds (Si-O bonds are always shorter than Al-O distances). q_{O} are the partial charges of oxygen atoms derived by the method of Hirshfeld.³⁵ f^+ and f^- are the condensed Fukui functions obtained with eqs 5 and 6, respectively. The bond valence parameters are calibrated on the basis of the structure of bulk pyrophyllite. The surface sites are shown in Figure 4a.

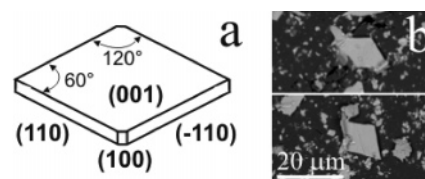
The observed energetic equivalence of the facets is consistent with simple crystal chemistry arguments of Pauling electrostatic valence principles and bond valence theory.^{37,41} On all facets, the Si surface sites are four-coordinated. Three Si-O bonds are similar to that in the bulk structure and contribute 3 valence units. The fourth bond is formed to the surface OH group and compensates the formal (+4) charge on the silicon. The Al edge sites are five-coordinated. The four bonds are identical to the bulk structure and contribute 2 valence units (0.5 valence units per bond). The fifth bond is different on various facets: Al-OH on the (010); Al-O-Si on (100) and (110); Al-O-Si and Al-OH on (130). Assuming that the formal charge of oxygen (-2) is equally distributed between O-Al and O-Si bonds or O-H and O-Al contacts, the formal (+3) charge of the surface Al polyhedron is exactly compensated by the bond valence.

The energy of the edges can be further reduced by physorption of molecular water. The H_2O molecules are attached to the Al sites to complete the octahedral coordination of surface aluminum (Figure 4b). The binding energy of the molecular water and the surface energies are summarized in Table 4. Interatomic distances on the surface are given in Table 6. Hereafter, these configurations are referred to as those with high

TABLE 6: Structural Parameters of the Surface Groups on Pyrophyllite at High Water Coverage ($4 \times \text{H}_2\text{O}$ per unit area)^a

	$\Sigma s_{\text{O-Me}}$	Me-O $R [\text{\AA}^2]/s_{ij}^{\text{DFT}}$	O-H $R [\text{\AA}^2]/s_{ij}^{\text{DFT}}$	q_{O}	f^-	f^+
(010)						
Si1-OH	1.963	1.658/0.931	0.976/0.913	-0.086	0.006	0.003
			2.062/0.120			
Si2-OH	1.893	1.640/0.976	0.986/0.885	-0.121	0.018	0.003
			2.726/0.033			
Al-OH	1.834	1.833/0.648	0.974/0.920	-0.149	0.040	0.002
			1.878/0.159			
			2.133/0.106			
Al-OH ₂	2.058	2.173/0.258	0.990/0.875	-0.016	0.005	0.004
(100)						
Si1-OH	1.874	1.660/0.925	0.972/0.924	-0.126	0.021	0.001
Si2-OH	1.992	1.668/0.907	0.976/0.913	-0.076	0.008	0.002
			1.647/0.230			
Al-OH ₂	2.191	2.064/0.348	0.995/0.864	0.011	0.002	0.003
			1.907/0.152			
Al-(OH)-Al	2.041	1.904/0.464	0.973/0.938	-0.078	0.007	0.003
Si-O-Al	1.887	1.609/1.061		-0.177	0.028	0.002
		1.815/0.680	2.207/0.095			
(110)						
Si1-OH	1.865	1.654/0.939	0.972/0.926	-0.131	0.021	0.001
Si2-OH	2.014	1.665/0.912	0.974/0.920	-0.068	0.003	0.002
			1.791/0.182			
Al-OH ₂	2.171	2.068/0.343	0.994/0.864	0.001	0.002	0.004
			0.980/0.902			
			2.446/0.061			
Al-(OH)-Al	1.946	1.926/0.503	1.923/0.508	-0.089	0.016	0.003
			0.975/0.917			
Si-O-Al	1.877	1.610/1.059	2.167/0.101	-0.184	0.037	0.001
		1.810/0.689				
(130)						
Si1-OH	1.922	1.636/0.987	0.973/0.922	-0.108	0.009	0.001
Si2-OH	1.948	1.651/0.947	0.972/0.924	-0.096	0.003	0.004
			2.322/0.077			
Si3-OH	1.866	1.653/0.943	0.972/0.923	-0.128	0.015	0.001
Si4-OH	1.886	1.648/0.954	0.974/0.920	-0.121	0.012	0.002
Al-OH ₂	2.130	2.029/0.384	0.996/0.864	-0.005	0.006	0.005
Al-OH	1.828	1.887/0.560	0.973/0.922	-0.137	0.032	0.002
			1.669/0.226			
			2.163/0.113			
	1.844	1.610/1.059	2.265/0.086	-0.178	0.031	0.001
		1.840/0.635				
Si-O-Al						
Al-(OH)-Al	1.980	1.883/0.565	0.975/0.917	-0.081	0.025	0.003
		1.930/0.498				

^a See Table 2 for details. The surface sites are shown in Figure 4b.

**Figure 5.** (a) The shape of pyrophyllite crystals predicted from surface energy calculations. (b) SEM images of well-shaped crystals of natural pyrophyllite.

water coverage. The energy of the water sorption on different edge facets (8–14 kcal/mol) significantly exceeds the typical energy of hydrogen bonds in liquid water⁴² (2.5–5.5 kcal/mol). Therefore, the geometry of the edges at high water coverage calculated for a surface exposed to the vacuum should be stable in the presence of water fluid. At high water coverage, the (110) and (100) facets are predicted to have much lower energy than the (010) and (130) facets. According to Wulff's method,⁴³ crystals of pyrophyllite should have a rhombic habit dominated by the (110) and (-110) forms (Figure 5a). The (100) facet gives a negligible contribution to the surface area of edges. In contrast to the commonly postulated hexagonal morphology of

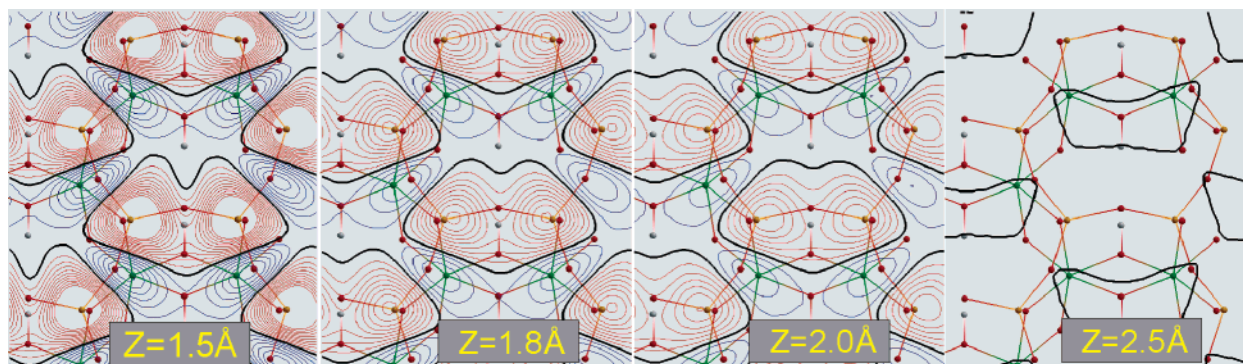


Figure 6. Contour plot of the ab initio electrostatic potential in the plane parallel to the (001) surface of pyrophyllite, 1.5, 1.8, 2.0, and 2.5 Å above the uppermost basal oxygen atom. Iso-lines are drawn for every 0.05 eV between -0.5 and $+0.5$ eV. The bold solid line is the iso-line of zero potential. Centers of negative potential (blue lines) are localized above the O^b1, O^b2, and OH sites, while the positive potentials (red lines) are concentrated above the silicon tetrahedra. Oxygen atoms are shown in red. The Al atoms are green. Si sites are light brown. Hydrogen atoms are gray.

clays, the (010) facet is not present in the crystal. To be stable, the surface energy of the (010) facet should be at least smaller than $3.2 \text{ meV}/\text{\AA}^2$, that is, far less than the calculated $5.4 \text{ meV}/\text{\AA}^2$. Natural pyrophyllite occurs as aggregates of irregularly shaped wafer. Well-formed crystals (Figure 5b) are extremely rare. The habit of well-shaped ones is consistent with our calculations. The form of well-shaped pallets is dominated by two facets having an angle close to 120° that suggests the (110) and (-110) indexing of these edges. The (130) and (-130) indexes can be ruled out because of their high surface energy predicted in the calculations. There were no particles with clear hexagonal shape found in the natural samples. Since the (110) and (-110) facets are most stable according to both calculation and observation in natural samples, the lateral surface area of irregularly shaped particles should be dominated by the (110) facet too.

Electrostatic Potential at (001) Plane of Pyrophyllite. The topology of the electrostatic potential near the surface of the clay particles provides an important guide for understanding the sorption behavior of mineral surfaces.⁴⁴ The electrostatic potentials near the (001) surface of talc and pyrophyllite were calculated by Bleam⁴⁵ on the basis of a classical point charge model. Molecular electrostatic potential maps for the $\text{FeSi}_4\text{O}_{14}\text{H}_{10}$ cluster were obtained by Chatterjee et al.⁴⁶ from the first-principle calculations. In Figure 6, we show a contour map of ab initio electrostatic potential parallel to the (001) surface of pyrophyllite at 1.5, 1.80, 2.0, and 2.5 Å above the uppermost basal oxygen atom (O^b1 and O^b2 sites). The potential was obtained from the supercell calculations of the periodic two-dimensional TOT units separated by 30 Å of vacuum in the *c* direction. The variation of the electrostatic potential above the basal oxygen and silicon atoms as function of distance in the [001] direction is shown in Figure 7.

The topology of the surface potential is mainly determined by rotation and tilting of the silicon tetrahedra. The surface geometry has a *cm* two-dimensional symmetry group. The potential is symmetric relative to the mirror plane passing through the OH dipoles. The basal oxygen atoms are subdivided into two nonequivalent sites. One-third of the basal oxygen atoms (O^b3 sites) are situated on the mirror plane. The O^b3 sites are slightly displaced toward the center of the TOT layer. The strong positive potential produced by neighboring silicon atoms screens the oxygen sites. Thus, Si–O^b3–Si groups form islands of positive electrostatic potentials. Figure 7 indicates that the potential above the O^b3 site reaches positive values at a distance of $\sim 1 \text{ \AA}$, passes through a maximum at 1.8 Å, and then asymptotically decays to zero. The O^b1 and O^b2 sites form the

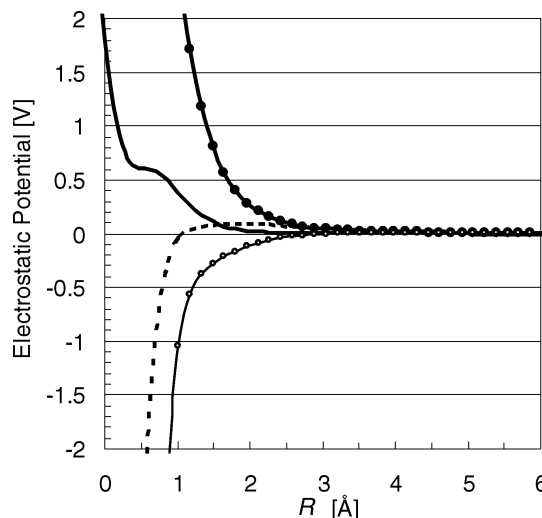


Figure 7. The variation of the electrostatic potential normal to the (001) plane of pyrophyllite. The filled circles indicate the potential directly above Si site, open circles indicate the potential above O^b1 or O^b2 sites, and the dashed line is the potential above O^b3 sites. The solid line shows the averaged electrostatic potential. The curves are meaningful only outside the core radius of pseudopotentials.

outermost atomic plane on the TOT surface. The electrostatic potential above those sites forms negative maxima situated on both sides of the mirror symmetry plane. The potential in the siloxane cavity shows a small negative value.

Since the TOT layer is electrically neutral and has inversion symmetry, the lowest possible multipole moment is a quadrupole, and the electrostatic potential should decay as r^{-8} . At 2.5 Å, the lateral variation of the potential is below 0.05 eV, and the lateral averaged potential approach a zero already at 2.0 Å from the outermost basal oxygen. Such a fast decay of the electrostatic interaction indicates that van der Waals forces might play a dominant role in the stacking of the TOT layers in pyrophyllite.

Unlike the (001) surface of talc,⁴⁵ the averaged electrostatic potential above the basal plane of the pyrophyllite has a small positive value. The difference in the sign of the electrostatic potential near pyrophyllite and talc suggests that the two minerals should show different sorption behavior with respect to positively and negatively charged ions. The basal plane of pyrophyllite is expected to interact more strongly with anions than cations.

The topology of the electrostatic potential on the basal plane is important for the development of sophisticated surface

complexation models on the basal plane of clay minerals. The potential map in Figure 6 is not limited to the pyrophyllite but can be used to predict the sorption behavior for a wide range of dioctahedral clays such as montmorillonite. It was shown⁴⁵ that the basic topology of the surface potential is dominated by contribution from the outermost tetrahedral layer. As a first approximation, the local structural distortion due to isomorphic substitution of Al^{3+} in the octahedral layer can be neglected. For the thermodynamic modeling of the sorption, the electrostatic potential can be expressed as a superposition of the idealized field of pyrophyllite (Figures 6, 7) and the average potential of the structural charge due to isomorphic substitution in the TOT layer.

Sorption of Water on (001) Surface of Pyrophyllite. The structure of the electrostatic potential near the pyrophyllite surface constrains the possible orientation of adsorbed water molecules. In a stable configuration, the hydrogen atoms of a water molecule would coincide with the negative surface potential, and the oxygen should be situated near the maxima of the positive potential. To find an optimal orientation of water near a pyrophyllite surface, a series of geometry optimizations with two water molecules per unit area ($5.219 \text{ \AA} \times 9.033 \text{ \AA}$) was performed. In the initial configurations, the water molecules were oriented parallel to the surface at about 2.0 \AA . Upon optimization, H_2O was found to migrate away from the surface to a distance of about 2.8 \AA . The water molecules are oriented in a plane nearly perpendicular to the surface. One of the OH bonds points to the center of the siloxane cavity or to the surface oxygen sites O^{b1} or O^{b2} . The oxygen atoms of water molecules are situated above the surface silicone atom. The dipole vector of H_2O is approximately parallel to the surface. The sorption energies of water molecules vary from 1.0 to 2.0 kJ/mol for different configurations. This is a rather small energy compared to the energy of the hydrogen bonding in the water. The results suggest that the uncharged basal plane of pyrophyllite should have hydrophobic features. This conclusion is in agreement with the previous studies of Bridgeman et al.,⁴⁷ who reported a positive energy for pyrophyllite swelling. The hydrophobic behavior of the basal plane in pyrophyllite was also suggested⁴⁸ on the basis of wettability measurements of a fresh pyrophyllite surface. A weak interaction of water molecules with the basal plane of pyrophyllite may facilitate water diffusion at the liquid–solid interface.

Sorption of Hydronium on (001) Surface of Pyrophyllite. In compacted systems, the proton sorption may buffer the pH equilibria in the interlayer water. It is therefore important to know the proton affinity of the mineral surface and the mechanism of proton sorption in order to correctly model the thermodynamic equilibria for compacted systems. According to the electrostatic potential above the basal plane of pyrophyllite (Figure 6), the proton may be situated above (O^{b1} , O^{b2}) oxygen sites or enter the siloxan cavity. To obtain the equilibrium configuration, several simulated annealing runs and direct geometry optimizations were performed starting with different initial orientations of the hydronium ion. Two configurations of the hydronium ion on the basal plane were found. In Figure 8, the proton is shared between the basal oxygen (O^{b1} , O^{b2}) and the water molecule (configuration I). The proton has a shorter distance to the basal plane than to the neighboring water, suggesting that the proton has a higher affinity to the surface than to water.

During MD simulations at 200 K , the structure remained stable. The shared proton was found to exchange between the

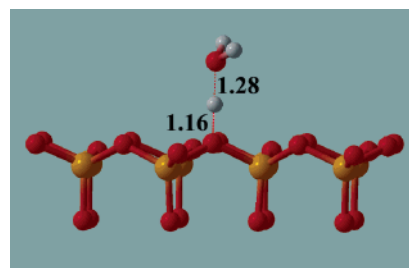


Figure 8. A possible sorption mechanism for the proton on the (001) plane of pyrophyllite. The proton is shared between water molecule and the O^{b1} or O^{b2} sites of the basal plane of pyrophyllite. The numbers are distances in angstroms. See Figure 1 for the color legend.

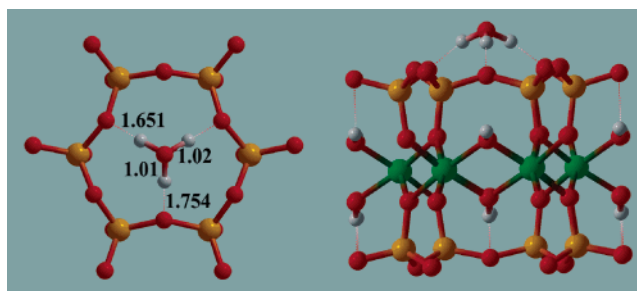


Figure 9. The most stable inner-sphere configuration of the hydronium on the basal plane of pyrophyllite. The numbers are distances in angstroms. See Figure 1 for the color legend.

surface and the adjacent water molecule. No energy barrier for the proton transfer could be observed. Such a behavior is similar to the dynamics of the H_5O_2^+ complex obtained by MD simulations with classical and quantum nuclei.⁴⁹ In the second configuration (Figure 9), the hydronium ion is situated parallel to the surface within the siloxane plane (configuration II). The ion dips into the siloxane cavity so that the oxygen atom is situated just 1.35 \AA above the outermost basal oxygen. Hydronium forms two strong hydrogen bonds with O^{b1} and O^{b2} sites. A somewhat weaker bond is directed to the O^{b3} site. In sufficiently long MD simulations at 300 K , the structure (I) was observed to rearrange into the structure (II) which remains stable at least for 5 ps . No proton transfer to the intrastructural OH group was observed.

Reactivity Indexes of the Edge Sites. The condensed Fukui functions have been used to predict the reactivity of functional groups in zeolites and clays.^{50,51} Calculated partial charges and reactivity indexes of surface oxygen sites on various facets of pyrophyllite are summarized in Tables 5 and 6. According to the local hard soft acid base principle,⁵² a site with maximal (minimal) Fukui function is preferred for a soft (hard) reaction. The surface is expected to behave as a soft acid. Thus, the oxygen sites with high partial charge and f^- index favor the protonation, whereas the sites with small partial charge and high f^+ index promote the deprotonation.

The highest values of f^- index (Tables 5, 6) suggest that the $\equiv\text{Al}-\text{OH}$ groups are most easily protonated on the (010) and (130) facets. The $\equiv\text{Al}-\text{O}-\text{Si}\equiv$ sites are to be protonated on (100), (130), and (110) surfaces. The electrophilic indexes f^+ show much smaller variations for different sites. At high water coverage (Table 6), $\equiv\text{Al}-\text{OH}_2$ sites undoubtedly correlate with very small negative to even positive partial charge of oxygen sites and higher values of f^+ , suggesting them to deprotonate first. At low water coverage (Table 5), f^+ values tend to be higher on $\equiv\text{Si}-\text{OH}$ sites, while the q_0 values are closer to zero for $\equiv\text{Al}-\text{OH}$ sites, indicating that both $\equiv\text{Si}-\text{OH}$ and $\equiv\text{Al}-\text{OH}$ sites should be able to deprotonate.

TABLE 7: Surface Site Densities SD [nm⁻²] and the Relative Enthalpies [kcal/mol] of Deprotonation/Protonation Reactions at Low Water Coverage^a

	SD	$\Delta H_{\text{calcd}}^{\text{dep}}$	$\Delta H_{\text{calcd}}^{\text{prt}}$	$\Delta H_{\text{pred}}^{\text{dep}}$	$\Delta H_{\text{pred}}^{\text{prt}}$
(010)					
Si1-OH	1.6	3	17	1	18
Si2-OH	1.6	-1		2	1
Al-OH	1.6		-17	6	-16
(100)					
Si1-OH	1.85	0	0	2	1
Si2-OH	1.85			0	22
Al-(OH)-Al	0.93	-7		-4	38
Si-O-Al	1.85		-17		-17
(110)					
Si1-OH	1.6	-4		1	22
Si2-OH	1.6	9	4	1	3
Al-(OH)-Al	1.6	-5		-2	25
Si-O-Al	1.6		-11		-27
(130)					
Si1-OH	0.93		24	0	23
Si2-OH	0.93	5		0	26
Si3-OH	0.93	5		1	11
Si4-OH	0.93			1	0
Al-OH	0.93	2	-16	6	-17
Si-O-Al	1.85				-28
Al-(OH)-Al	0.93			-2	22

^a The $\Delta H_{\text{calcd}}^{\text{dep}}$ and $\Delta H_{\text{calcd}}^{\text{prt}}$ values are obtained from direct optimization of the surface geometry. The $\Delta H_{\text{pred}}^{\text{dep}}$ and $\Delta H_{\text{pred}}^{\text{prt}}$ values are predicted using eqs 16 and 18. The surface sites are shown in Figure 4a. The protonation/deprotonation energies of the $\equiv\text{Si1-OH}$ site in the (100) surface are used as the reference enthalpy (see text for details).

Relative Protonation/Deprotonation Enthalpies of Edge Sites. The reactivity indexes and population analysis provide a good guess for reactive surface sites. The more accurate probe should not only be based on the electronic properties of the reactants but also take into account structural and electronic transformations in the reaction products. One of the possible options is the direct calculation of the relative protonation/deprotonation enthalpies in the gas phase. Several geometry optimization runs have been performed to obtain the relative protonation enthalpy of $\equiv\text{Al-OH-Al}\equiv$, $\equiv\text{Al-O-Si}\equiv$, $\equiv\text{Si-OH}$, and $\equiv\text{Al-OH}$ surface groups and the energy of deprotonation reactions for $\equiv\text{Al-OH-Al}\equiv$, $\equiv\text{Al-OH}_2$, $\equiv\text{Si-OH}$, and $\equiv\text{Al-OH}$ sites at different crystallographic facets and water coverage. It turned out that not all protonation and deprotonation constants can be extracted. For example, on the facet (010) at high water coverage, all initial configurations tried have converged to deprotonation of the $\equiv\text{Al-OH}_2$ group, proving that the deprotonation of the other sites on (010) facets is strongly unfavorable as long as $\equiv\text{Al-OH}_2$ remains protonated. For the surface with several sites having substantially different binding energies, the deprotonation occurs stepwise. The weakest sites deprotonate first, and only then do the stronger sites come into play. The importance of the structural changes during successive deprotonation steps has been clearly illustrated by Bickmore et al.¹⁹ for the (100) facet of cristobalite.

The relative protonation/deprotonation enthalpies that could be obtained by direct structure optimization are summarized in Tables 7 and 8 for the low and high water coverage, respectively. These values are calculated as the difference between the total energies of the optimized protonated/deprotonated surfaces and that of the respective neutral edges. The protonated/deprotonated surfaces contain the same number of electron but excess/lack of one proton relative to the neutral system, respectively. Thus, the protonated and deprotonated systems are charged. The charged periodic systems are treated using an auxiliary homo-

TABLE 8: Surface Site Densities SD [nm⁻²] and Relative Enthalpies [kcal/mol] of Deprotonation/Protonation Reactions at High Water Coverage^a

	SD	$\Delta H_{\text{calcd}}^{\text{dep}}$	$\Delta H_{\text{calcd}}^{\text{prt}}$	$\Delta H_{\text{pred}}^{\text{dep}}$	$\Delta H_{\text{pred}}^{\text{prt}}$
(010)					
Si1-OH	1.6			-12	9
Si2-OH	1.6			-7	-2
Al-OH	1.6		-20	-2	-19
Al-OH ₂	1.6	-70		-23	14
(100)					
Si1-OH	1.85	0	0	-6	-4
Si2-OH	1.85		-1	-14	8
Al-OH ₂	1.85	-24		-27	18
Al-(OH)-Al	0.93	-9		-13	9
Si-O-Al	1.85		-19		-12
(110)					
Si1-OH	1.6		0	-5	-5
Si2-OH	1.6		17	-15	12
Al-OH ₂	1.6	-31		-26	17
Al-(OH)-Al	1.6			-12	2
Si-O-Al	1.6		-17		-19
(130)					
Si1-OH	0.93			-9	5
Si2-OH	0.93			-11	10
Si3-OH	0.93	-14		-6	0
Si4-OH	0.93			-7	2
Al-OH ₂	1.85	-25		-25	14
Al-OH	1.85			-4	-13
Si-O-Al	1.85		-13		-15
Al-(OH)-Al	1.85			-13	-4

^a The $\Delta H_{\text{calcd}}^{\text{dep}}$ and $\Delta H_{\text{calcd}}^{\text{prt}}$ values are obtained from direct optimization of the surface geometry. The $\Delta H_{\text{pred}}^{\text{dep}}$ and $\Delta H_{\text{pred}}^{\text{prt}}$ values are predicted using eqs 15 and 17. The surface sites are shown in Figure 4b. The protonation/deprotonation energies of the $\equiv\text{Si1-OH}$ site in the (100) surface are used as the reference enthalpy (see text for details).

geneous background charge used to ensure the charge neutrality of the simulated system. Such a method has been proven to be efficient for studying the redox reactions and the ion solvation in condensed media.^{53,54} The technique implies, however, that the energy differences between neutral and protonated/deprotonated surfaces contain spurious self-interaction of the electron density and the pseudoatoms with the neutralizing background. Because the volume of the supercell is similar in all calculations, the charge density of the neutralizing background is the same in all system setups. Therefore, one can assume that the self-interaction term gives approximately the same constant contribution to the calculated protonation or deprotonation enthalpies of the surface sites. It is not possible, however, to make a precise estimate of the self-interaction term. Although the calculated enthalpies are valid within a constant, the relative surface protonation/deprotonation enthalpies are accurate within an assumption of the similar dielectric properties of the surface geometries. To measure the relative acidity of the surface sites, the reference energy for the protonation/deprotonation reactions can be arbitrarily taken. To remove uncertainty due to the self-interaction term, we set the protonation and deprotonation enthalpies of the $\equiv\text{Si1-OH}$ site in the (100) surface to zero. This choice of the reference system is purely arbitrary and taken by convenience only. The all protonation/deprotonation enthalpies reported in Tables 7 and 8 are measured relative to that of the $\equiv\text{Si1-OH}$ site on the (100) surface with the respective water coverage.

The relative acidities of the surface groups obtained from direct calculation of the deprotonation enthalpies are in good agreement with predictions based on Fukui functions, partial charges, and the bond valence sum on the surface oxygen sites.

According to the calculated relative enthalpies of protonation, $\equiv\text{Al}-\text{O}-\text{Si}\equiv$ sites must have the highest proton affinity on (100), (110), and (130) facets and $\text{Al}-\text{OH}$ groups on the (010) facet at high water coverage. Indeed, the electrophilic index f_i^- is maximal for those sites (Table 6). Similarly, the $\equiv\text{Al}-\text{OH}_2$ are to be deprotonated first, because the q_{O} is close to zero or even positive and the f_i^+ is maximal. Similar correlations were found for low water coverage, showing that the Fukui functions and the partial charges are good indicators of the site reactivity on the surfaces of pyrophyllite. The observed relative acidity of the surface sites is also in agreement with the predictions of the bond valence theory. On all the studied facets, the bond valence sums have the smallest values on the surface oxygen sites with the highest proton affinity. Similarly, the sites with the lowest proton affinity are characterized by the highest bond valence sum.

Since the relative protonation/deprotonation enthalpies of surface sites correlate with the Stockholder charges and Fukui indexes, it can be used to estimate the protonation/deprotonation energies of the surface complexes where the direct estimation of enthalpies was not successful. Because the Fukui functions are determined within a normalization factor, the Fukui indexes for the different surface sites should be compared within the single calculation. To compare the reactivity of the different facets, the local softness should be used. On the basis of the fact that different facets were simulated using the same number of atoms (electrons) and the studied surfaces were in equilibrium with the same bulk material, the results from Fukui indexes for different sites can still be comparable. For the protonation reaction, a very strong correlation was found for two-parameter linear relationships

$$\Delta H_{\text{pred}}^{\text{prt}} [\text{kcal/mol}] = 18.5 + 64.69q_{\text{O}} - 699.14f_i^- \quad (15)$$

$$\Delta H_{\text{pred}}^{\text{prt}} [\text{kcal/mol}] = 57.3 + 296.67q_{\text{O}} - 744.23f_i^- \quad (16)$$

applied to high (eq 15) and low (eq 16) water coverage, respectively.

Both partial charges and f_i^+ correlate with the relative enthalpy of the deprotonation reaction. The combination of q_{O} and f_i^+ does not improve the correlation, however. Therefore, only q_{O} was used to predict relative deprotonation enthalpies. Two linear regressions obtained for deprotonation at high (eq 17) and low (eq 18) water coverage, respectively, are as follows:

$$\Delta H_{\text{pred}}^{\text{dep}} [\text{kcal/mol}] = -25.6 - 155.848q_{\text{O}} \quad (17)$$

$$\Delta H_{\text{pred}}^{\text{dep}} [\text{kcal/mol}] = -9.1 - 90.1557q_{\text{O}} \quad (18)$$

The predicted relative protonation/deprotonation enthalpies are summarized in Tables 7 and 8. The different equations have to be used for the high and low water coverage, because the Fukui index calculations derived from the calculations with different numbers of electrons cannot be treated simultaneously. The surfaces with high water coverage have more freedom for structural rearrangements that minimize the energy of the system after protonation/deprotonation. The structural relaxations on the surfaces with high water coverage partly mimic the solvation effects on the effects on the fluid-surface interface.

The 1:1 correlation between $\Delta H_{\text{pred}}^{\text{dep}}$ and $\Delta H_{\text{pred}}^{\text{prt}}$ estimated from the direct calculations of relative protonation/deprotonation enthalpies and the predictions based on eqs 15–18 are given in Figure 10. The correlation is reasonably good except for a

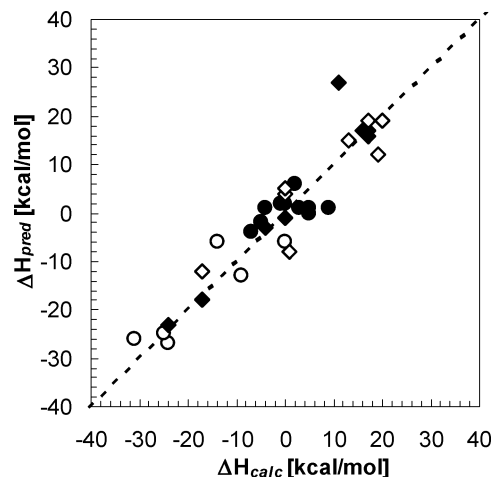


Figure 10. 1:1 correlation between the directly calculated relative protonation/deprotonation enthalpies of the surface sites and the predicted ones from eqs 15–18. Open symbols and filled symbols stand for surfaces with high and low water coverage, respectively. The values of (ΔH^{dep}) are given by circles. The $(-\Delta H^{\text{prt}})$ values are given by diamonds. The enthalpies are measured relative to the protonation/deprotonation enthalpies of the $\equiv\text{Si1}-\text{OH}$ site in the (100) surface (see text for detail).

single point (deprotonation of the $\text{Al}-\text{OH}_2$ site on the (010) facet). The discrepancy for $\text{Al}-\text{OH}_2$ sites is believed to be due to the complex structural relaxations on the (010) surface that significantly reduce the deprotonated energy of $\text{Al}-\text{OH}_2$ sites.

Acidity Scale for the Edge Sorption Sites. Several methods have been proposed to predict acidity of the surface groups on edge sites based on ab initio calculations and the crystal chemistry.^{18–20} The weak and strong sides of such methods have been discussed in detail by Bickmore et al.¹⁹ Most of the models try to predict the pK of the surface sites based on the energy–bond strength relationships of the reactants without considering structural relaxations in the reaction products. This approach on one hand significantly reduces the computational efforts but on the other hand neglects the structural relaxations in the reaction products that can be important in complex systems. The ab initio calculations offer a possibility of calculating directly the relative protonation and deprotonation enthalpies of the surface sites that would take into account structural relaxations both in reactants and products.

Systematic studies of the ion solvated energies and the proton affinities in the gas phase show that the acidities of the solvated molecules can be approximately deduced from the gas-phase deprotonation enthalpies.⁵⁵ Because the protonation/deprotonation entropy is small compared to enthalpy,⁵⁶ the gas-phase acidities at room temperature can be approximated by gas-phase deprotonation enthalpy alone. The effects of the solvation are mainly to reduce the relative differences in the acidities of the different functional groups.⁵⁶

In Figure 11, calculated deprotonation enthalpies in a vacuum for various oxyacids are shown against experimental pK values at room temperature.⁵⁷ The deprotonation enthalpies are obtained using a supercell calculation similar to that used for the edge sites of pyrophyllite. It is worth mentioning that the calculated deprotonation enthalpies are in agreement with experimental data within of few kilocalories per mole (the comparison is not shown). This indicates that the self-interaction of the positively charged proton and negatively charged deprotonated acid with the neutralizing charge background used in the supercell calculation of charged systems cancel each other out. The plot shows a clear linear relationship between relative protonation

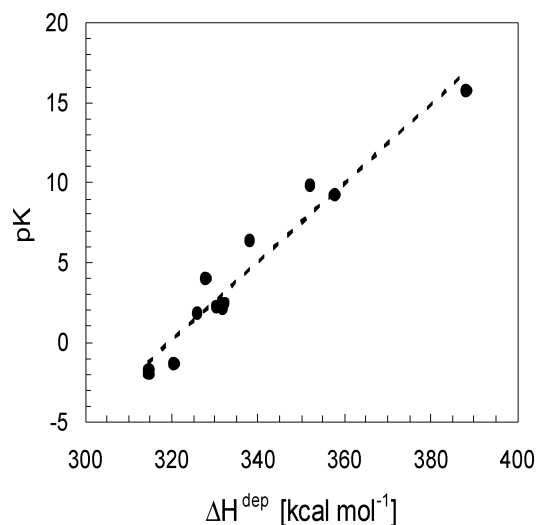


Figure 11. Correlation between calculated relative enthalpy (ΔH^{dep}) of the first deprotonation step of various oxyacids (H_2SO_4 , H_3PO_4 , $\text{H}_3\text{-AsO}_4$, H_3VO_4 , H_4SiO_4 , HNO_3 , H_3BO_3 , H_2SO_3 , H_2O , H_2CO_3 , H_2SeO_4 , H_2SeO_3) in the gas phase and the experimental pK values⁵⁷ at room temperature in the solution.

enthalpy in the gas phase and the pK value in the solution. The scatter of the points can be explained by a difference in the molecular geometry, solvation effects, and different mechanisms of the structural relaxations in the deprotonated molecules. Although the deviations of the points on the order of 2 pK units look huge, such accuracy would be a rather good estimation for the acidities of the reactive sites on the complex surface. Thus, if an empirical linear correlation exists for the oxyacids, one can expect a similar linear relationship to hold between the protonation/deprotonation enthalpies of the surface sites and their acidities in the solution

$$\text{pK}_{\text{edge}} = \text{C1}_{\text{edge}} * \Delta H^{\text{dep}} + \text{C2}_{\text{edge}} \quad (19)$$

where C1_{edge} and C2_{edge} are unknown parameters to be determined. Thus, eq 19 combined with the experimental data for the titration of pyrophyllite and the predicted structure of the edge sites give a way to construct a physically valid thermodynamic model for sorption on the clays.⁵⁸ In such a model, ab initio simulations provide the structure, the density, and the relative acidities for the complexes on the edge site on pyrophyllite, while the calculated surface energies predict the relative stabilities and occurrence of different edge facets.

The estimation of the surface site acidities based on eq 19 has many similarities with the methods based on the bond length–bond strength relationships. Figure 12 illustrates that partial charges on the oxygen surface sites correlate with the bond valence sum on the surface sites. Bickmore et al.^{19,20} used the bond valence method to predict pK for deprotonation of surface sites based on linear correlations obtained for oxyacids in aqueous solution. In our method, we linearly relate the Stockholder charges to the relative deprotonation enthalpy (eqs 17, 18). Since the linear relationship between valence sum and partial charges exists, both methods are mathematically equivalent and suffer from the same shortcomings: (1) there is an implicit consideration of the structural relaxation on the protonated/deprotonated surfaces (eqs 15–18); (2) the model does not take into account stepwise protonation/deprotonation events; (3) mineral-specific parameters for eq 19 and solvation effects are unknown. The first and second drawback can be eliminated by direct modeling of the stepwise protonation/deprotonation

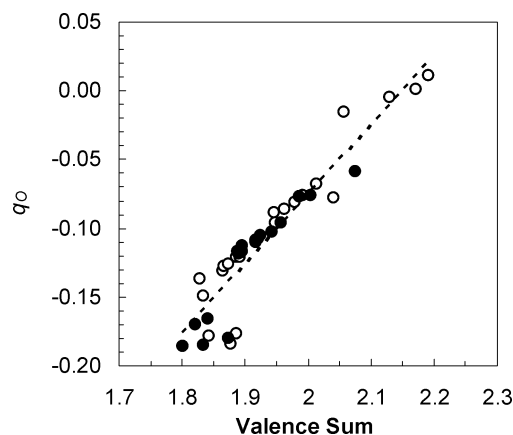


Figure 12. Correlation between Stockholder charges on the oxygen atoms (q_{O}) of various surface groups vs valence sum ($\sum_j s_{ij}$) on oxygen atoms (eqs 7, 8). Filled symbols are the values for low water coverage; the results for the high water coverage are represented by open circles.

reactions. The third flaw could be removed if the parameters of the linear relationship in eq 19 were independently determined from experimental data for the mineral of interest. In such a way, the internally consistent relationship between theoretically calculated relative protonation/deprotonation enthalpies and the pK of the surface sites in clays can be obtained.

Conclusion

The structure and electrostatic properties of pyrophyllite have been modeled using an orthorhombic supercell. The results of our calculations are in excellent agreement with available experimental data for pyrophyllite and sophisticated ab initio simulations. It was shown that the symmetry-constrained model is able to reproduce basic structural characteristic of pyrophyllite accurately.

The electrostatic potential near the (001) surface of pyrophyllite was used to analyze possible scenarios for water sorption on the basal plane of pyrophyllite. The calculations predict slightly hydrophobic behavior of the basal plane. Contrary to the talc, the average electrostatic potential above the (001) of pyrophyllite has a small positive value. The hydronium ion was found to enter the siloxane cavity and form a strong inner-sphere complex on the basal plane.

The relative stability and composition of lateral facets of the pyrophyllite have been calculated. The studied facets were found to have similar surface energies at low water coverage. For the high water coverage, (110) and (-110) are predicted to dominate over other facets. On the basis of the Fukui functions and the relative protonation/deprotonation enthalpies, the acidity of the edge sites has been predicted. The $\equiv\text{Al}-\text{O}-\text{Si}\equiv$ sites have the highest proton affinity on (100), (110) and (130) facets and $\text{Al}-\text{OH}$ groups on the (010) edges. The deprotonation of the $\equiv\text{Al}-\text{OH}_2$ sites is followed by $\equiv\text{Al}-\text{OH}$ and $\equiv\text{Si}-\text{OH}$ groups. The most serious weakness of the models used to predict the protonation constants of the surface sites, including our work, is the absence of an internal calibration for the surface of specific minerals. The accurate values of pK could be obtained by combining experimental data on titration of clay minerals combined with the relative stabilities of the surface sites predicted by ab initio calculations.

Acknowledgment. The simulations have been performed using CPMD v3.9 package on the IBM-SP4 in the CSCS. The data processing and visualization have been done with the AVS-Express package. The author is grateful to Marcella Iannuzzi

and Dmitry Kulik for a fruitful discussion. Special thanks go to Mario Valle for his help in the visualization of the results. The SEM images of natural pyrophyllite were kindly provided by Fatima Gonzalez.

References and Notes

- (1) Grim, R. E. *Clay Mineralogy*, 2nd ed.; McGraw-Hill: New York, 1968.
- (2) Skipper, N. T.; Chang, F. R. C.; Sposito, G. *Clays Clay Miner.* **1995**, *43*, 285.
- (3) Skipper, N. T.; Sposito, G.; Chang, F. R. C. *Clays Clay Miner.* **1995**, *43*, 294.
- (4) Boek, E. S.; Coveney, P. V.; Skipper, N. T. *Langmuir* **1995**, *11*, 4629.
- (5) Whitley, H. D.; Smith, D. E. *J. Chem. Phys.* **2004**, *120*, 5387.
- (6) Chatterjee, A.; Ebina, T.; Onodera, Y.; Mizukami, F. *J. Chem. Phys.* **2004**, *120*, 3414.
- (7) Marry, V.; Turq, P.; Cartailier, T.; Levesque, D. *J. Chem. Phys.* **2002**, *117*, 3454.
- (8) Bickmore, B. R.; Bosbach, D.; Hochella, M. F.; Charlet, L.; Rufe, E. *Am. Mineral.* **2001**, *86*, 411.
- (9) Bosbach, D.; Charlet, L.; Bickmore, B. R.; Hochella, M. F. *Am. Mineral.* **2000**, *85*, 1209.
- (10) Oelkers, E. H. *Geochim. Cosmochim. Acta* **2001**, *65*, 3703.
- (11) White, G. N.; Zelazny, L. W. *Clays Clay Miner.* **1988**, *36*, 141.
- (12) Bradbury, M. H.; Baeyens, B. *J. Contam. Hydrol.* **1997**, *27*, 223.
- (13) Bradbury, M. H.; Baeyens, B. *J. Contam. Hydrol.* **2000**, *42*, 141.
- (14) Bradbury, M. H.; Baeyens, B. *Geochim. Cosmochim. Acta* **2005**, *69*, 875.
- (15) Bradbury, M. H.; Baeyens, B. *Geochim. Cosmochim. Acta* **1999**, *63*, 325.
- (16) Tournassat, C.; Ferrage, E.; Poinsignon, C.; Charlet, L. *J. Colloid Interface Sci.* **2004**, *273*, 234.
- (17) Tournassat, C.; Greneche, J. M.; Tisserand, D.; Charlet, L. *J. Colloid Interface Sci.* **2004**, *273*, 224.
- (18) Hiemstra, T.; Riemsdijk, W. H. v. *J. Colloid Interface Sci.* **1996**, *179*, 488.
- (19) Bickmore, B. R.; Tadanier, C. J.; Rosso, K. M.; Monn, W. D.; Eggett, D. L. *Geochim. Cosmochim. Acta* **2004**, *68*, 2025.
- (20) Bickmore, B. R.; Rosso, K. M.; Nagy, K. L.; Cygan, R. T.; Tadanier, C. J. *Clays Clay Miner.* **2003**, *51*, 359.
- (21) Geerlings, P.; Proft, F. D.; Langenaeker, W. *Chem. Rev.* **2003**, *103*, 1793.
- (22) Hohenberg, P.; Kohn, W. *Phys. Rev.* **1964**, *136*, 864.
- (23) Kohn, W.; Sham, L. J. *Phys. Rev.* **1965**, *140*, A1133.
- (24) Perdew, J. P.; Burke, K.; Ernzerhof, M. *Phys. Rev. Lett.* **1996**, *77*, 3865.
- (25) Vanderbilt, D. *Phys. Rev. B* **1990**, *41*, 7892.
- (26) Car, R.; Parrinello, M. *Phys. Rev. Lett.* **1985**, *55*, 2471.
- (27) Lee, J. H.; Guggenheim, S. *Am. Mineral.* **1981**, *66*, 350.
- (28) MacKenzie, K. J. D.; Brown, I. W. M.; Meinhold, R. H.; Bowden, M. E. *J. Am. Ceram. Soc.* **1985**, *68*, 266–272, 266.
- (29) Refson, K.; Park, S. H.; Sposito, G. *J. Phys. Chem. B* **2003**, *107*, 13376.
- (30) Hochney, R. W. Potential calculation and some applications. In *Methods in Computational Physics*; Academic Press: New York, 1970; Vol. 9, p 136.
- (31) Parr, R. G.; Pearson, R. G. *J. Am. Chem. Soc.* **1983**, *105*, 7512.
- (32) Li, Y.; Evans, J. N. S. *J. Am. Chem. Soc.* **1995**, *117*, 7756.
- (33) Yang, W.; Mortier, W. J. *J. Am. Chem. Soc.* **1987**, *108*, 5708.
- (34) Löwdin, P. O. *Phys. Rev.* **1955**, *97*, 1490.
- (35) Hirshfeld, F. L. *Theor. Chim. Acta* **1977**, *44*, 129.
- (36) Roy, R. K.; Pal, S.; Hirao, K. *J. Chem. Phys.* **1999**, *110*, 8236.
- (37) Brown, I. D. *The Chemical Bond in Inorganic Chemistry: The Bond Valence Model*; Oxford University Press: Oxford, 2002.
- (38) Karki, B. B.; Stixrude, L.; Clark, S. J.; Warren, M. C.; Ackland, G. J.; Crain, J. *Am. Mineral.* **1997**, *82*, 635.
- (39) Allmann, R. *Monatsh. Chem.* **1975**, *106*, 779.
- (40) Bleam, W.; Welhouse, G.; Janowiak, M. *Clays Clay Miner.* **1993**, *41*, 305.
- (41) Pauling, L. *J. Am. Chem. Soc.* **1929**, *51*, 1010.
- (42) Kalinichev, A. G.; Bass, J. D. *Chem. Phys. Lett.* **1994**, *231*, 301.
- (43) Zangwill, A. *Physics at Surfaces*; Cambridge University Press: New York, 1988.
- (44) Aray, Y.; Marquez, M.; Rodríguez, J.; Coll, S.; Simón-Manso, Y.; Gonzalez, C.; Weitz, D. A. *J. Phys. Chem. B* **2003**, *107*, 8946.
- (45) Bleam, W. F. *Clays Clay Miner.* **1990**, *38*, 522.
- (46) Chatterjee, A.; Iwasaki, T.; Ebina, T.; Hayashi, H. *J. Mol. Graphics* **1996**, *14*, 302.
- (47) Bridgeman, C. H.; Buckingham, A. D.; Skipper, N. T.; Payne, M. C. *Mol. Phys.* **1996**, *89*, 879.
- (48) Schader, M. E.; Yariv, S. *J. Colloid Interface Sci.* **1990**, *136*, 85.
- (49) Tuckerman, M. E.; Marx, D.; Klein, M. L.; Parrinello, M. *Science* **1997**, *275*, 817.
- (50) Chatterjee, A.; Iwasaki, T.; Ebina, T. *J. Phys. Chem. A* **2000**, *104*, 8216.
- (51) Chatterjee, A.; Iwasaki, T.; Ebina, T. *J. Phys. Chem. A* **1999**, *103*, 2489.
- (52) Pearson, R. G. *J. Chem. Educ.* **1987**, *64*, 561.
- (53) Tuckerman, M.; Laasonen, K.; Sprik, M.; Parrinello, M. *J. Phys. Chem.* **1995**, *99*, 5749.
- (54) Blumberger, J.; Bernasconi, L.; Tavernelli, I.; Vuilleumier, R.; Sprik, M. **2004**, *126*, 3928.
- (55) Meot-Ner, M. *J. Phys. Chem.* **1987**, *91*, 417.
- (56) Meot-Ner, M. *Int. J. Mass Spectrom.* **2003**, *227*, 525.
- (57) *CRC Handbook of Chemistry and Physics*, 85th ed.; CRC Press: Boca Raton, 2004–2005.
- (58) Kulik, D. A.; Churakov, S. V. Clays in Natural and Engineered Barriers for Radioactive Waste Confinement. 2th International meeting; 2005; p 605.